

# Quasi-two-dimensional convection in a three-dimensional laterally heated box in a strong magnetic field normal to main circulation

Alexander Yu. Gelfgat<sup>1</sup> and Sergei Molokov<sup>2</sup>

<sup>1</sup>*Faculty of Engineering, School of Mechanical Engineering, Tel-Aviv University, Ramat Aviv, Tel-Aviv 69978, Israel*

<sup>2</sup>*Applied Mathematics Research Centre, Coventry University, Priory Street, Coventry CV1 5FB, United Kingdom*

(Received 2 August 2010; accepted 30 November 2010; published online 1 March 2011)

Convection in a laterally heated three-dimensional box affected by a strong magnetic field is considered in the quasi-two-dimensional (Q2D) formulation. It is assumed that the magnetic field is strong and is normal to the main convective circulation. The stability of the resulting Q2D flow is studied for two values of the Hartmann number scaled by half of the width ratio, 100 and 1000, and for either thermally insulating or perfectly conducting horizontal boundaries. The aspect length-to-height ratio of the box is varied continuously between 4 and 10. It is shown that the magnetic field damps the bulk flow and creates thermal and Shercliff boundary layers at the boundaries, which become the main source of instabilities. In spite of the general tendency of the flow stabilization by the magnetic field, the flow instability takes place in different ways depending on the boundary conditions and the aspect ratio. Similarities with other magnetic field directions and flows with larger Prandtl numbers are discussed. © 2011 American Institute of Physics.

[doi:10.1063/1.3549932]

## I. INTRODUCTION

Buoyant magnetoconvection plays a fundamental role in various natural phenomena, such as geo- and solar dynamo, as well as in many industrial applications. Magnetoconvection is also very interesting from a fundamental point of view as it exhibits a variety of nonlinear effects: a sequence of bifurcations of various kind, symmetry breaking, transition to chaos, pattern formation, etc.<sup>1–5</sup>

For magnetoconvection in industrial applications, such as fusion reactor blankets, semiconductor crystal growth, and electromagnetic processing of materials,<sup>4–16</sup> a problem of fundamental importance is convection in a rectangular box filled with an electrically conducting fluid, and with one of the vertical walls being heated, while another one being cooled.

Examples of electrically conducting fluids include liquid metals, such as Hg, Na, NaK, and GaInSn, widely used in a laboratory (or Li and PbLi used in nuclear fusion). Thermophysical properties of liquid semiconductors (Si, Ge, and many compound semiconductors) are very close to those of liquid metals. Both groups of materials are characterized by large electrical conductivity of the order of  $10^6 \Omega^{-1} \text{ m}^{-1}$  and a small Prandtl number of the order of  $10^{-2}$ .

The flow takes place in the presence of an applied uniform magnetic field, which results in magnetohydrodynamic (MHD) interaction in the bulk of the flow. This interaction makes the flow highly anisotropic with flow structures being extended along the magnetic field, and results in a strong damping of three-dimensional velocity disturbances leaving only those lying in the plane normal to the magnetic field. As a rule, MHD flows remain three-dimensional as the presence of electrically conducting walls, slight misalignment of the

field with the parallel walls, development of the velocity profile, etc. result in significant three-dimensional effects, especially if the so-called parallel layers are involved. Examples of such flows include buoyant convection in a cavity in a vertical and transverse magnetic fields,<sup>4,8,13–17</sup> flows with Hunt's jets,<sup>18–21</sup> flows in bends,<sup>22,23</sup> circular ducts in a non-uniform magnetic field,<sup>24,25</sup> etc.

In some situations, usually involving a pair of parallel electrically insulating walls transverse to the sufficiently strong magnetic field, the flow becomes quasi-two-dimensional (Q2D). Such flows are characterized by a very small or zero velocity along the field, a distinct core where the fluid flows in a quasi-two-dimensional manner, in the planes transverse to the field, and thin Hartmann layers whose role is mainly to provide linear damping for the core velocity.<sup>26</sup>

Models of Q2D flows have been developed for the flow between parallel planes in a uniform magnetic field,<sup>27,28</sup> a nonuniform magnetic field,<sup>29,30</sup> or buoyant convection in a uniform field.<sup>7,8,11,12</sup> More elaborate Q2D models have been developed by Pothérat *et al.*,<sup>31,32</sup> which take into account small but finite Ekman pumping in the Hartmann layers.

Here we will be dealing with the flow in a laterally heated long three-dimensional box with electrically insulating walls in the presence of a strong horizontal magnetic field directed normally to both gravity and the initial temperature gradient [Fig. 1(a)]. The Q2D model used here has already been successful in predicting the linear stability for the Rayleigh–Bénard problem for an infinite layer with periodic boundary conditions in the axial direction,<sup>11</sup> as well as for the isothermal mixing layer.<sup>33</sup> However, we revisit the derivation of the Q2D model to stress the importance of exact local conservation laws. After that we describe our nu-

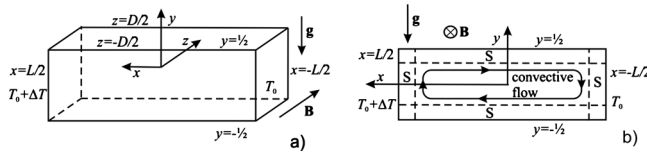


FIG. 1. Schematic diagram of buoyant convection in a horizontal magnetic field with horizontal temperature gradient: (a) three-dimensional cavity; (b) two-dimensional cavity for the averaged flow with respect to  $z$  and the position of the averaged Shercliff layers  $S$  of thickness  $O(\text{Ha}^{-1/2})$ .

merical results on the flow patterns and their stability. In this study, we focus on the effect of the Hartmann number and the aspect ratio of the box on linear stability threshold.

The configuration considered is similar to those studied experimentally and numerically in Refs. 13–16; however, it assumes significantly larger Hartmann numbers for which the Q2D model is applicable. Note that comparing the results of two-dimensional (2D) stability of convection in long horizontal cavities with experimental data (without the magnetic field), Gelfgat *et al.*<sup>34</sup> argued that the 2D model yields reliable results for width ratios larger than 5. Here we show that, contrary to the flows unaffected by a strong transverse magnetic field, the latter makes the role of vertical walls in the third direction crucial for the stability of the flow even when the width ratio is considerably large. Depending on the magnetic field strength and thermal boundary conditions imposed on the horizontal boundaries of the cavity, we observe three main instability modes. The perturbation patterns show that in a strong magnetic field the instability develops in the boundary layers adjacent to the vertical and horizontal walls. In weaker magnetic field and with perfectly conducting horizontal boundaries, the instability develops in the bulk of the flow similar to the cases when the magnetic field is absent.

## II. FORMULATION

Consider the convective flow of a fluid of electrical conductivity  $\sigma$ , kinematic viscosity  $\nu$ , thermal diffusivity  $\kappa$ , and density  $\rho = \rho_0[1 - \beta(T^* - T_0^*)]$ , where  $\beta$  is the thermal expansion coefficient and  $\rho_0$  is the fluid density at temperature  $T_0^*$ . The flow takes place in a three-dimensional rectangular box with electrically insulating walls in the presence of a horizontal magnetic field  $\mathbf{B} = B_0 \mathbf{e}_z$ , as shown in Fig. 1(a). Here  $(x, y, z)$  are Cartesian coordinates. The height, length, and width of the box are  $H^*$ ,  $L^*$ , and  $D^*$ , respectively. The walls of the box at  $x = \mp L^*/2$  are kept at constant values of temperature  $T_0^*$  and  $T_0^* + \Delta T^*$ , respectively, while those at  $z = \pm D^*/2$  are thermally insulating.

In the Boussinesq approximation, the dimensionless equations governing the flow are<sup>12</sup>

$$\nabla^2 \mathbf{v} + \text{Ha}^2 \mathbf{j} \times \mathbf{e}_z = \nabla p - \text{Gr} T \mathbf{e}_y + (\mathbf{v} \cdot \nabla) \mathbf{v} + \frac{\partial \mathbf{v}}{\partial t}, \quad (1)$$

$$\mathbf{j} = -\nabla \phi + \mathbf{v} \times \mathbf{e}_z, \quad (2)$$

$$\nabla \cdot \mathbf{v} = 0, \quad (3)$$

$$\nabla \cdot \mathbf{j} = 0, \quad (4)$$

$$\text{Pr}^{-1} \nabla^2 T = (\mathbf{v} \cdot \nabla) T + \frac{\partial T}{\partial t}, \quad (5)$$

where  $t$  is the time,  $\mathbf{v} = (u, v, w)$  is the fluid velocity,  $p$  is the pressure,  $\mathbf{j}$  is the electric current density, and  $\phi$  is the electric potential, normalized using the scales  $H^{*2}/\nu$ ,  $\nu/H^*$ ,  $\rho_0 \nu^2/H^{*2}$ ,  $\sigma B_0 \nu/H^*$ , and  $B_0 \nu$ , respectively. The temperature is rendered dimensionless by  $T = (T^* - T_0^*)/\Delta T^*$ . Above, the dimensionless parameters are  $\text{Ha} = B_0 H^* (\sigma/\rho_0 \nu)^{1/2}$ ,  $\text{Gr} = \rho_0 g \beta \Delta T H^{*3}/\nu^2$ , and  $\text{Pr} = \nu/\kappa$ : the Hartmann, Grashof, and Prandtl numbers, respectively. In fusion reactor blankets, parameters  $\text{Ha}$  and  $\text{Ha}d$  defined below vary in the range of  $10^3 - 10^4$ . In all the calculations below, the value of the Prandtl number was fixed to  $\text{Pr} = 0.015$ . This value is a characteristic of liquid metals and semiconductors and was used in several previous studies (see, e.g., Refs. 5 and 34 and references therein).

The boundaries are no-slip and electrically insulating, which implies

$$\mathbf{v} = 0, \quad (6a)$$

$$\mathbf{j} \cdot \hat{\mathbf{n}} = 0 \quad \text{at all the walls.} \quad (6b)$$

The thermal boundary conditions are

$$T = 0 \quad \text{at } x = -L/2, \quad (7)$$

$$T = 1 \quad \text{at } x = L/2, \quad (8)$$

$$\partial T / \partial z = 0 \quad \text{at } z = \pm D/2, \quad (9)$$

and either

$$T = 1/2 + x/L \quad \text{at } y = \pm 1/2 \quad (10)$$

or

$$\partial T / \partial y = 0 \quad \text{at } y = \pm 1/2 \quad (11)$$

for thermally conducting or insulating horizontal walls, respectively. Above,  $\hat{\mathbf{n}}$  is the normal unit vector to a wall, and  $L = L^*/H^*$  and  $D = D^*/H^*$  are aspect and width ratios of the box, respectively.

## III. AVERAGING IN THE DIRECTION NORMAL TO THE MAIN CIRCULATION

We assume that the magnetic field is sufficiently strong to make the flow Q2D and derive the governing equations for the quantities averaged in the  $z$  direction, normal to the main convective circulation that takes place in the  $(x, y)$  plane.

The first step is averaging the Ohm's law for the component of current transverse to the field and the continuity equations. This gives

$$\bar{\mathbf{j}}_{\perp} = -\nabla_{\perp} \bar{\phi} + \bar{\mathbf{v}}_{\perp} \times \mathbf{e}_z, \quad (12)$$

$$\nabla_{\perp} \cdot \bar{\mathbf{v}}_{\perp} = 0, \quad (13)$$

$$\nabla_{\perp} \cdot \bar{\mathbf{j}}_{\perp} = 0, \quad (14)$$

where

$$\bar{F} = \frac{1}{D} \int_{-D/2}^{D/2} F(x, y, z, t) dz \quad (15)$$

is the  $z$ -average for any quantity  $F(x, y, z, t)$ , the subscript  $\perp$  denotes the projection of a vector onto the  $(x, y)$ -plane, which is transverse to the magnetic field.

Taking the  $z$ -component of *curl* of Eq. (12) and using Eq. (13) yields

$$\nabla_{\perp} \times \bar{\mathbf{j}}_{\perp} = 0. \quad (16)$$

Equations (14) and (16) imply that the average transverse current is both solenoidal and irrotational, and together with the boundary condition  $\bar{\mathbf{j}}_{\perp} \cdot \hat{\mathbf{n}} = 0$  for electrically insulating sidewalls at  $x = \pm L/2$  and  $y = \pm 1/2$ , this yields

$$\bar{\mathbf{j}}_{\perp} = 0. \quad (17)$$

In particular, this implies that for a uniform magnetic field, there are no loops of total current in the  $(x, y)$ -cross-section. This is in contrast to, say, a developing flow in a duct with a nonuniform magnetic field, where such loops are of utmost importance for shaping the velocity profile.<sup>29</sup>

It follows from Eq. (12) with  $\bar{\mathbf{j}}_{\perp} = 0$  that the average electric potential is the stream function for the averaged velocity, i.e.,

$$\bar{\mathbf{v}}_{\perp} = \nabla_{\perp} \times (\bar{\phi} \mathbf{e}_z) = \mathbf{e}_z \times \nabla_{\perp} \bar{\phi}, \quad (18)$$

and that

$$\nabla_{\perp}^2 \bar{\phi} = \bar{\omega}_{\parallel}, \quad (19)$$

where  $\bar{\omega}_{\parallel} = \mathbf{e}_z \cdot (\nabla_{\perp} \times \bar{\mathbf{v}}_{\perp})$  is the component of the average vorticity in the direction of the field. Note that the electric potential gradient is the quantity normally measured in the experiments.

The flow properties between plane electrically insulating walls given by Eqs. (16)–(19) are of particular importance as they are exact, local, independent of the Hartmann or Reynolds numbers, and are valid for both laminar and turbulent flows. They are not related to the properties of the Hartmann layer, as the only assumption made for the derivation of these relations is that the boundaries are nonpenetrable and electrically insulating. Thus, these equations equally hold, for example, for a layer with fixed, free, electrically insulating boundaries. For solid, no-slip boundaries at  $z = \pm D/2$  equation (17) immediately implies that once the core and the Hartmann layers are established, they carry equal and opposite current, a property which is often derived by elaborate arguments involving the properties of the Hartmann layer.

Next, we average the Navier Stokes equation (1) projected onto the  $(x, y)$ -plane and use the continuity equation (3) and the nonpenetration condition in Eq. (6a). This results in

$$\begin{aligned} \nabla_{\perp}^2 \bar{\mathbf{v}}_{\perp} + \left. \frac{\partial \mathbf{v}_{\perp}}{\partial z} \right|_{z=D/2} - \left. \frac{\partial \mathbf{v}_{\perp}}{\partial z} \right|_{z=-D/2} \\ = \nabla_{\perp} \bar{p} - \text{Gr} \bar{T} \mathbf{e}_y + \overline{(\mathbf{v}_{\perp} \cdot \nabla_{\perp}) \mathbf{v}_{\perp}} + \overline{\mathbf{v}_{\perp} (\nabla_{\perp} \cdot \mathbf{v}_{\perp})} + \frac{\partial \bar{\mathbf{v}}_{\perp}}{\partial t}. \end{aligned} \quad (20)$$

We further assume that  $\mathbf{v}_{\perp}(x, y, z, t) = \bar{\mathbf{v}}_{\perp}(x, y, t)h(z)$ , where

$$\begin{aligned} h(z) \cong \frac{\text{Ha}}{D \text{Ha} - 2} \{1 - \exp(\text{Ha}[z - D/2]) \\ - \exp(-\text{Ha}[z + D/2])\} \end{aligned} \quad (21)$$

is the asymptotic Hartmann profile for  $\text{Ha} \gg 1$  with  $\overline{h(z)} \cong 1$ . According to this assumption, the term  $\overline{\mathbf{v}_{\perp} (\nabla_{\perp} \cdot \mathbf{v}_{\perp})}$  is of the order of  $O(\text{Ha}^{-1})$ . Retaining only the terms of the leading order for  $\text{Ha} \gg 1$  yields the momentum equation for the average quantities as follows:

$$\nabla_{\perp}^2 \bar{\mathbf{v}}_{\perp} - \text{Hd} \bar{\mathbf{v}}_{\perp} = \nabla_{\perp} \bar{p} - \text{Gr} \bar{T} \mathbf{e}_y + (\bar{\mathbf{v}}_{\perp} \cdot \nabla_{\perp}) \bar{\mathbf{v}}_{\perp} + \frac{\partial \bar{\mathbf{v}}_{\perp}}{\partial t}, \quad (22)$$

where  $\text{Hd} = 2 \text{Ha}/D$  is the Hartmann number scaled by a half of the width ratio. In Eq. (22), the contribution of the inertial terms by averaging  $\overline{h^2(z)}$  is of the order of  $O(\text{Ha}^{-1})$ . These terms have been neglected as it is normally done with the averaged Q2D flow models.

Concerning Eq. (22), it is the two-dimensional momentum equation with linear damping, which is a result of viscous friction in the Hartmann layers adjacent to the walls at  $z = \pm D/2$ . This term is similar to the Darcy law in porous fluids, the analogy already explored by Burr *et al.*<sup>11</sup>

Averaging the energy equation yields

$$\begin{aligned} \text{Pr}^{-1} \left[ \nabla_{\perp}^2 \bar{T} + \left. \frac{\partial T}{\partial z} \right|_{z=D/2} - \left. \frac{\partial T}{\partial z} \right|_{z=-D/2} \right] \\ = \overline{(\mathbf{v}_{\perp} \cdot \nabla_{\perp}) T} + \overline{T (\nabla_{\perp} \cdot \mathbf{v}_{\perp})} + \frac{\partial \bar{T}}{\partial t}. \end{aligned} \quad (23)$$

Since the lateral walls at  $z = \pm D/2$  are thermally insulating,  $\partial T / \partial z(z = \pm D/2) = 0$ , and the  $z$ -component of velocity is much smaller than the other two, the terms  $v_z \partial T / \partial z$  and  $\partial^2 T / \partial z^2$  are assumed to be much smaller than other terms of the energy equation. Therefore, the temperature field is assumed to be independent of  $z$ , which implies that  $T = \bar{T}(x, y, t)$ . Then Eq. (23) becomes

$$\text{Pr}^{-1} \nabla_{\perp}^2 \bar{T} = (\bar{\mathbf{v}}_{\perp} \cdot \nabla_{\perp}) \bar{T} + \frac{\partial \bar{T}}{\partial t}. \quad (24)$$

Equations (13), (22), and (24), omitting subscript  $\perp$  and overbar, yield the two-dimensional equations for the averaged quantities as follows:

$$\nabla^2 \mathbf{v} - \text{Hd} \mathbf{v} = \nabla p - \text{Gr} T \mathbf{e}_y + (\mathbf{v} \cdot \nabla) \mathbf{v} + \frac{\partial \mathbf{v}}{\partial t}, \quad (25)$$

$$\nabla \cdot \mathbf{v} = 0, \quad (26)$$

$$\text{Pr}^{-1} \nabla^2 T = (\mathbf{v} \cdot \nabla) T + \frac{\partial T}{\partial t}. \quad (27)$$

Equations (25)–(27) are solved together with the boundary conditions (6a), (7), and (8), and either Eq. (10) or Eq. (11), in a two-dimensional cavity shown in Fig. 1(b). Burr and Müller<sup>11</sup> argued that the Q2D model is justified if the flow in the central region, close to  $z=0$ , is uniform in the direction of magnetic field  $z$ , and the Hartmann layer thickness is independent of the core variables to the main order of approximation, which resulted in the two conditions  $\text{Ra}/\text{Ha}^2 \ll 1$  and  $\text{Pr Ha}^2 \ll 1$ . Here,  $\text{Ra}$  is the Rayleigh number,  $\text{Ra}=\text{Gr Pr}$ . Note that according to our notations,  $\text{Ha}=\text{Hd}D/2$ . Therefore, for each value of  $\text{Hd}$  we can find the width ratio  $D$  large enough to satisfy both conditions.

To perform the linear stability analysis, the flow variables are split into the steady base flow and the infinitesimally small perturbations as follows:

$$\{u, v, p, T\} = \{U, V, P, \Theta\} + \{\tilde{u}, \tilde{v}, \tilde{p}, \tilde{\theta}\} e^{\lambda t},$$

where  $\lambda$  is the complex increment, and all the functions on the right-hand side depend on  $x$  and  $y$  only. Substituting these expressions into Eqs. (25)–(27) and linearizing for small perturbations, we arrive at the linear stability problem

$$\nabla^2 \tilde{\mathbf{v}} - \text{Hd} \tilde{\mathbf{v}} = \nabla \tilde{p} - \text{Gr} \tilde{\theta} \mathbf{e}_y + (\mathbf{V} \cdot \nabla) \tilde{\mathbf{v}} + (\tilde{\mathbf{v}} \cdot \nabla) \mathbf{V} + \lambda \tilde{\mathbf{v}}, \quad (28)$$

$$\nabla \cdot \tilde{\mathbf{v}} = 0, \quad (29)$$

$$\text{Pr}^{-1} \nabla^2 \tilde{\theta} = (\mathbf{V} \cdot \nabla) \tilde{\theta} + (\tilde{\mathbf{v}} \cdot \nabla) \Theta + \lambda \tilde{\theta}. \quad (30)$$

The linear stability analysis yields the value of critical Grashof number  $\text{Gr}_{\text{cr}}$ , at which there exists a (leading) eigenvalue that changes the sign of its real part from negative (stability) to positive (instability). For the problem considered here, it appears as a complex conjugate pair, which corresponds to a transition from steady to oscillatory flow states, as a rule, via the Hopf bifurcation. The imaginary part of the leading eigenvalue, called critical frequency  $\omega_{\text{cr}}$ , yields an approximation of circular frequency of slightly supercritical oscillations. In the case of the Hopf bifurcation, the eigenvector corresponding to the leading eigenpair yields additional information on the pattern of the appearing flow oscillations. Its absolute value corresponds to the distribution of the oscillation amplitude, while its real and imaginary values represent instantaneous deviation of the oscillating flow from the corresponding unstable steady state (see, for example, Refs. 34–37). Note also that the linear stability analysis yields the amplitude or deviation only to within multiplication by a constant, so that only relative values are physically meaningful. Following the common notation, we call the eigenvector corresponding to the leading eigenvalue the most unstable perturbation, or just a perturbation.

TABLE I. Critical Rayleigh number for Rayleigh–Bénard problem affected by a transverse magnetic field calculated analytically (Ref. 11) and numerically (present) for the Q2D model. Here,  $\text{Ra}=\text{Gr Pr}$  is the Rayleigh number.

Hd	$\alpha$	$\text{Ra}_{\text{cr,numerical}}$	$\text{Ra}_{\text{cr,analytical}}$
0	2.2214	657.541	657.511
100	2.9226	4699.373	4699.1355
1000	3.1119	40 256.050	40 253.99

#### IV. NUMERICAL METHOD AND TEST CALCULATIONS

Equations (25)–(30) are discretized by the standard finite volume technique. Steady states are calculated by Newton iteration with parameter continuation where necessary. The eigenvalues of Eqs. (28)–(30) are computed using the shift-and-inverse formulation with Arnoldi iteration. We use the direct sparse matrix solver MUMPS to inverse the Jacobian matrices as well as to calculate Krylov bases. The details of the numerical technique are given in Ref. 37.

Since the numerical technique was verified for  $\text{Ha}=\text{Hd}=0$  in Ref. 37, here we test the correctness of the numerical formulation by the comparison with the analytical results of Burr and Müller,<sup>11</sup> and then examine the convergence of critical parameters for several values of the scaled Hartmann number and the aspect ratio.

To reproduce the analytical results of Burr and Müller,<sup>11</sup> we consider the stability of quiescent state in a rectangular cavity whose horizontal boundaries are stress-free and are maintained at different temperatures. Periodicity conditions are imposed at the vertical boundaries. The length of the cavity is taken to be equal to the critical wavelength  $2\pi/\alpha$ , which corresponds to the onset of instability in an infinite horizontal layer. The comparison is shown in Table I. The calculation was done using  $300 \times 300$  stretched finite volume grid. It follows that using 300 nodes in each spatial direction yields four correct decimal digits, which completes the verification of consistency of the numerical model.

The convergence of the numerical scheme is illustrated in Fig. 2 for the aspect ratio  $L=4$  and 10 and scaled Hartmann number  $\text{Hd}=0, 100$ , and 1000. Calculations were done by varying the number of grid points in vertical direction  $N_y$  between 30 and 250 for  $L=4$  and between 50 and 300 for  $L=10$ . The number of grid points in the horizontal direction  $N_x$  was then defined as  $N_x=N_y L$ . It should be mentioned that the recent benchmark calculations of Gelfgat<sup>37</sup> showed that to achieve convergence in calculations of critical parameters, it is necessary to use grids having about  $10^2$  nodes in the shortest spatial direction. Also, it was stated earlier that calculations of convective flows affected by a magnetic field are more difficult than that without electromagnetic effects.<sup>5</sup> The present test calculations support these two conclusions. As it is seen in Fig. 2, with the increase of the scaled Hartmann number, the convergence of the critical Grashof number slows down. In the most numerically difficult cases, at  $\text{Hd}=1000$ , the difference between the critical Grashof numbers calculated for  $N_y=200$  and 300 is within 1% (Fig. 2), which we consider as a good convergence. In

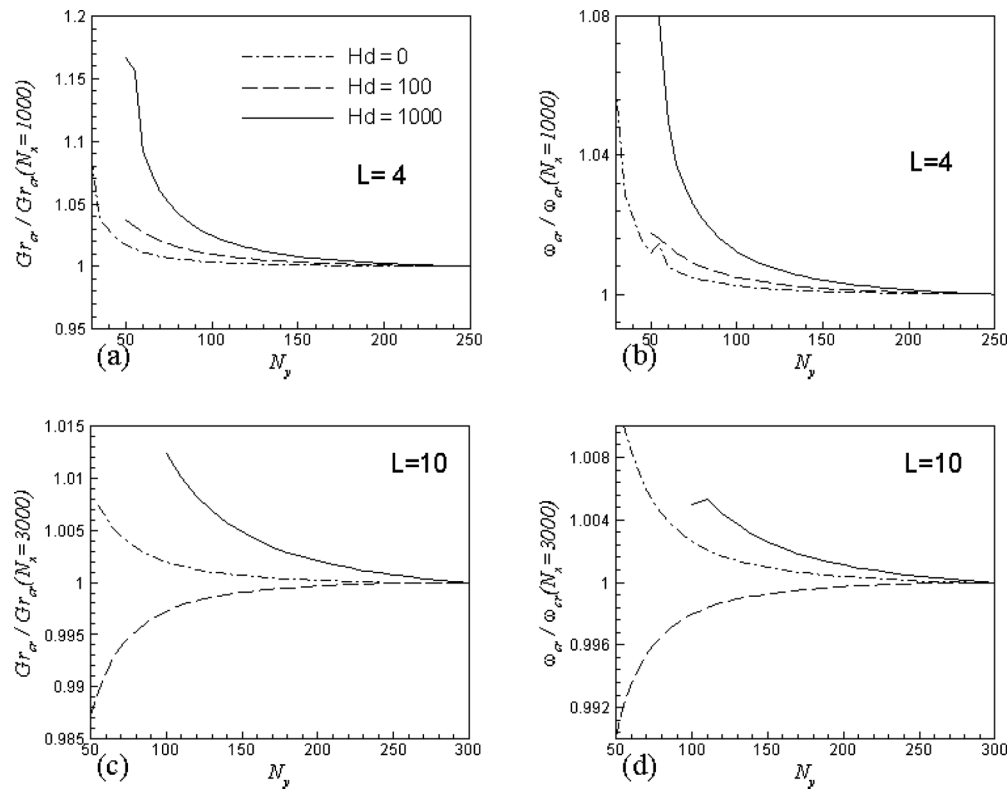


FIG. 2. Convergence of the critical Grashof number and critical frequency with the grid refinement. Thermally insulated horizontal boundaries.  $Pr=0.015$ .

the following calculations, we fixed  $N_y=200$  and defined  $N_x$  as above ( $N_x=N_yL$ ).

The Q2D model applied for the Rayleigh–Bénard configuration was successfully compared with the experimental measurements in Ref. 11, which validated the Q2D model. Since our numerical results completely agree with those of Burr and Müller<sup>11</sup> (Table I), it is clear that our comparison with their experiment is exactly the same. A more demanding comparison can be done with the experimental results of Burr *et al.*,<sup>15</sup> who reported the values of Rayleigh numbers  $Ra$  corresponding to the appearance of oscillations in the flow. These results were reported for a tall cavity with  $L=0.1$  as critical values of  $Ra$  versus the magnetic parameter  $M$ , which are connected with the present notations as  $Ra=Gr Pr L^3$  and  $M=HdLD/2$ . The reported experimental results state that for  $M=400, 800$ , and  $1600$ , the oscillations are observed at  $Ra=10^4, 4 \times 10^4$ , and  $8 \times 10^4$ , respectively. The present calculations reach the values of the critical Rayleigh number  $650, 2.2 \times 10^4$ , and  $4.3 \times 10^4$  for, respectively, the same values of  $M$ . For further comparison, we must take into account that the experimental critical values are clearly not precise. According to Fig. 4 of Ref. 15, the parameter  $M$  was varied there just by doubling its value starting from  $M=100$ . Therefore, the numerical critical numbers, which correspond to zero oscillation amplitude, must be smaller than those reported in Ref. 15. Thus, the comparison made can be considered as a qualitative agreement.

## V. RESULTS

Examples of streamlines and isotherms of steady state flows for  $Hd=100$  and  $1000$  are shown in Figs. 3 and 4 for, respectively, the cases of perfectly insulating and perfectly

conducting horizontal boundaries. As is usually defined for flows in enclosures, the stream function attains the zero value at the boundaries. With variation of the aspect ratio, the flow patterns remain similar to those shown for  $L=4$  and  $10$  and change continuously between these two patterns. Similar to the magnetic field applied in two other directions,<sup>5</sup> the transverse magnetic field suppresses the multiplicity of steady states observed by Gelfgat *et al.*<sup>34</sup> Also, contrary to flows unaffected by magnetic field,<sup>35</sup> the change of heat transfer properties of the horizontal boundaries drastically affects the flow pattern. The results related to convective flows in cavities without magnetic field effect, as well as some of the results related to magnetic field applied in two

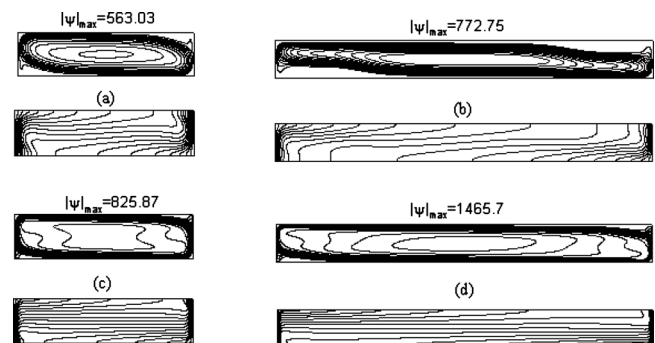


FIG. 3. Streamlines (upper frames) and isotherms (lower frames) of steady flows at critical values of the Grashof number. Perfectly insulated horizontal boundaries. All the isolines are equally spaced.  $Pr=0.015$ . (a)  $L=4$ ,  $Hd=100$ ,  $Gr_{cr}=1.80 \times 10^7$ ; (b)  $L=10$ ,  $Hd=100$ ,  $Gr_{cr}=3.69 \times 10^7$ ; (c)  $L=4$ ,  $Hd=1000$ ,  $Gr_{cr}=3.00 \times 10^8$ ; (d)  $L=10$ ,  $Hd=1000$ ,  $Gr_{cr}=1.13 \times 10^9$ .

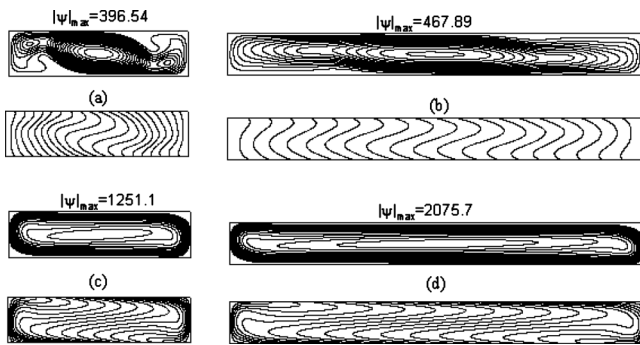


FIG. 4. Streamlines (upper frames) and isotherms (lower frames) of steady flows at critical values of the Grashof number. Perfectly conducting horizontal boundaries. All the isolines are equally spaced.  $Pr=0.015$ . (a)  $L=4$ ,  $Hd=100$ ,  $Gr_{cr}=4.28 \times 10^6$ ; (b)  $L=10$ ,  $Hd=100$ ,  $Gr_{cr}=6.42 \times 10^6$ ; (c)  $L=4$ ,  $Hd=1000$ ,  $Gr_{cr}=1.22 \times 10^8$ ; (d)  $L=10$ ,  $Hd=1000$ ,  $Gr_{cr}=3.37 \times 10^8$ .

other directions, are summarized in the recent book of Lappa<sup>2</sup> to which the reader is referred.

In the case of perfectly insulated horizontal boundaries, the isotherms are orthogonal to them, which allows the development of thin thermal boundary layers near the vertical walls. Together with the thermal boundary layers, we observe thin velocity boundary layers adjacent to all four boundaries. These are Shercliff (or parallel) boundary layers,<sup>9</sup> which become thinner with the increase of the magnetic field. The changes in flow patterns, compared to those developing in the absence of the magnetic field, are similar to the effect of increasing viscosity, or increasing the Prandtl number. On the other hand, the streamline and isotherm patterns shown in Fig. 3 are similar to those observed in the vertical and horizontal magnetic fields at much lower values of the Hartmann number.<sup>4</sup>

The perfectly conducting boundaries do not allow the development of thermal boundary layers at the vertical walls [Figs. 4(a)–4(c)]. Again, this is similar to what was observed for convection of fluids with a larger Prandtl number. With the increase of the magnetic field, boundary layers start to develop, but are significantly thicker than in the case of insulated boundaries. As shown below, the existence or absence of developed boundary layers has a decisive effect on the flow stability properties.

### A. Stability for perfectly insulated horizontal boundaries

Neutral curves showing the dependence of the critical Grashof number on the aspect ratio  $Gr_{cr}(L)$ , together with the dependencies  $\omega_{cr}(L)$ , are shown in Fig. 5 for  $Hd=100$  and 1000. With variation of the aspect ratio  $L$ , the instability is caused by different perturbation modes that, within the linear stability framework, abruptly replace each other. This is similar to other cases of convection in cavities when one of the governing parameters is varied (see, e.g., Refs. 2, 5, and 34 and references therein). To illustrate that the dependence of the eigenvalues on the governing parameters is continuous, variation of several eigenvalues belonging to the leading part of the spectrum along the neutral curves with increasing  $L$  is shown in frames (e) and (f) of Fig. 5. Parts of the curves

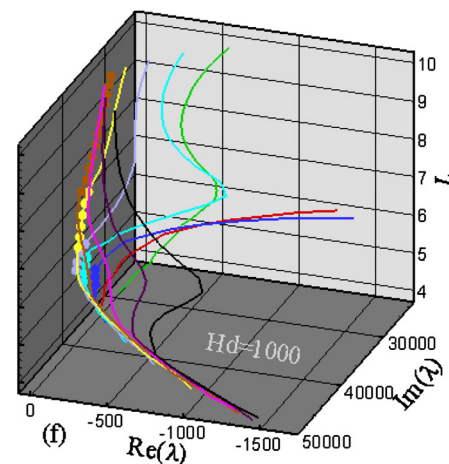
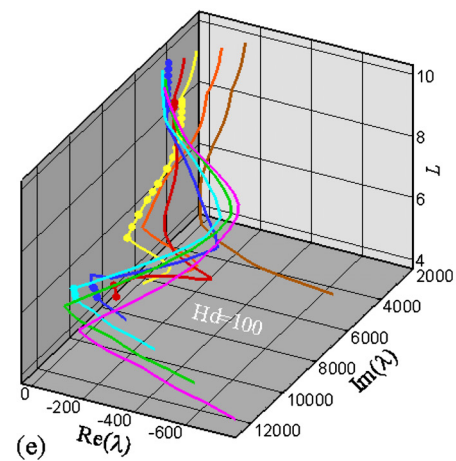
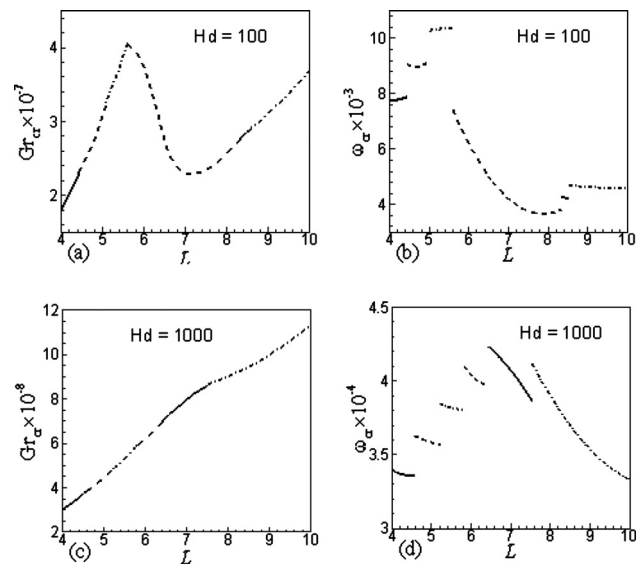


FIG. 5. (Color online) Critical Grashof numbers and critical frequencies for oscillatory instability of steady flows in the case of perfectly thermally insulated horizontal boundaries. Different line patterns correspond to different instability modes.  $Pr=0.015$ . Frames (e) and (f) show how eigenvalues change along the neutral curves with variation of  $L$ , circles indicate places where the eigenvalue is leading.

where the eigenvalue becomes leading are indicated by circles. Clearly, all the most unstable perturbation modes are the eigenvectors of the linearized stability problem whose eigenvalues cross the imaginary axis before others at a given

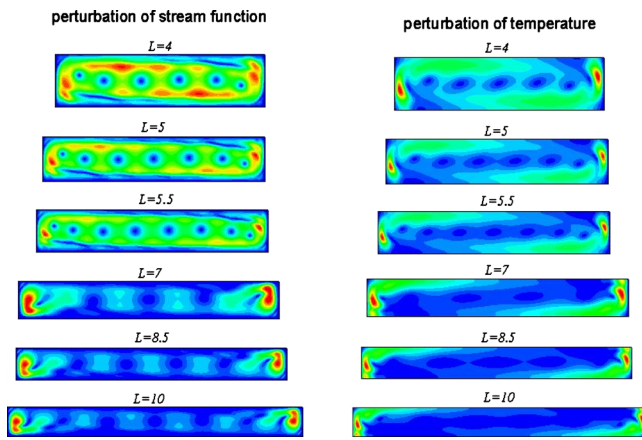


FIG. 6. (Color online) Absolute values of perturbation of stream function and temperature at  $Hd=100$  and aspect ratios corresponding to different branches of the neutral curve. Perfectly insulated horizontal boundaries. Red (gray) color corresponds to the maximal values, blue (black) color corresponds to the zero values.  $Pr=0.015$ .

set of the governing parameters. Unfortunately, in most cases, as well as for the problem considered here, it is not possible to offer a clear explanation or description of instability reasons or mechanisms. Trying to avoid unnecessary speculations, here we describe only the computed perturbation patterns, point on the analogies with already studied configurations, and offer only few explanatory arguments on what is observed. It should be emphasized also that in a supercritical flow regime, one can expect interaction of several unstable perturbation modes, whose eigenvalues crossed the imaginary axis at close values of the Grashof number.

According to Ref. 34, in the absence of the magnetic field, the single-cell flows become unstable at  $Gr_{cr} \approx 1.32 \times 10^5$ , which is two orders of magnitude less than the minimal value of Fig. 5(a). Many-cell convective flows can remain stable at significantly larger Grashof numbers; however, as discussed above (see also Figs. 3 and 4), these patterns are suppressed by the magnetic field. A comparison with the results of Gelfgat *et al.*<sup>34</sup> obtained in the absence of magnetic field shows that the spanwise magnetic field suppresses the many-cell patterns, so that the single-cell flow becomes a single steady state.

The critical Grashof number grows with the increase of  $Hd$  [cf. Figs. 5(a) and 5(c)]. In the considered range  $4 \leq L \leq 10$ , at both values of  $Hd$ , we observe six different eigenmodes that are most unstable at different aspect ratios. The jumps of critical frequency in Figs. 5(b) and 5(d) correspond to the changes of modes, as shown by the symbols in Fig. 5. At the same time, a closer look at the eigenmode patterns shows that not all modes at  $Hd=100$  and 1000 are similar. Absolute values of the eigenvectors, i.e., the most unstable perturbations, are shown in Figs. 6 and 7 for  $Hd=100$  and 1000, respectively. The red color corresponds to the maximal values and the blue color corresponds to the zero values.

For  $Hd=100$  (Fig. 6) and for smaller aspect ratios,  $4 \leq L \leq 5.6$ , the perturbation patterns are characterized by steep maxima of the temperature perturbations located near the vertical walls. Approximately at the same location, we

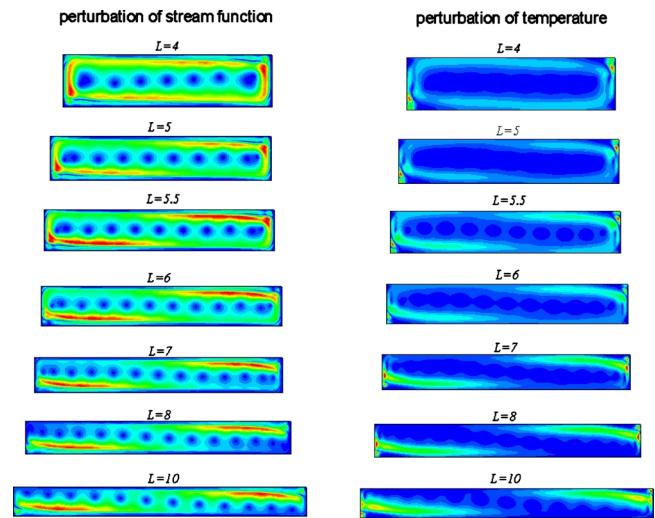


FIG. 7. (Color online) Absolute values of perturbation of stream function and temperature at  $Hd=1000$  and aspect ratios corresponding to different branches of the neutral curve. Perfectly insulated horizontal boundaries. Red (gray) color corresponds to the maximal values, blue (black) color corresponds to the zero values.  $Pr=0.015$ .

observe the maxima of the stream function (or velocity) perturbations; however, there are other two large perturbation areas stretched along the horizontal boundaries. Together with these strongly perturbed areas we observe, both in the stream function and temperature perturbation patterns, a “street” of local minima in the central part of the cavity. The number of minima changes abruptly with the increase of the aspect ratio, which exactly corresponds to the replacement of the leading perturbation mode. At the same time, with the increase of the aspect ratio, the secondary maxima located near the horizontal walls weaken and almost disappear at  $L=5.5$ . Note that the three patterns shown for  $L=4, 5$ , and  $5.5$  in Fig. 6 belong to different eigenvectors of the linearized stability problem. At the same time, their apparent similarity allows us to argue that all of them result from the same instability mechanism, which is illustrated below in more detail.

For  $L > 5.6$  and  $Hd=100$  (Fig. 6), the perturbation pattern changes qualitatively. Again, we observe three distinct instability modes, while a similarity of their patterns shows that they are triggered by the same physical reasons. As before, we observe large temperature perturbations near the vertical walls. The maxima of the stream function perturbation located near the vertical walls significantly grow, while the number of minima located in the central part of the cavity sharply decreases. Thus, by a change of the aspect ratio from  $L=5.5$  to  $L=5.7$ , we observe that eight local minima of stream function perturbation and seven of the temperature perturbation are replaced by, respectively, three and two minima. This pattern remains unchanged up to  $L=8.3$ . Starting from  $L=8.4$ , we again observe replacements of leading eigenmodes, which again are characterized by an abrupt increase of the number of local minima (Fig. 5 for  $L=8, 8.5$ , and 10).

For  $Hd=1000$  (Fig. 7) the perturbation patterns are similar to those observed in Fig. 5 for smaller aspect ratios and

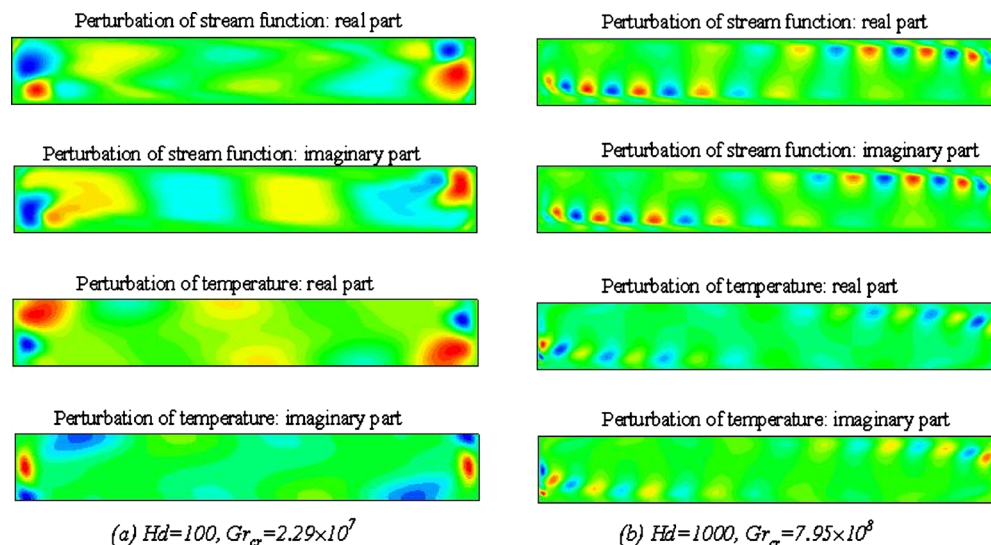


FIG. 8. (Color online) Real and imaginary parts of the stream function and temperature perturbations at  $L=7$ .  $Pr=0.015$ . (enhanced online). [URL: <http://dx.doi.org/10.1063/1.3549932.1>] [URL: <http://dx.doi.org/10.1063/1.3549932.2>] [URL: <http://dx.doi.org/10.1063/1.3549932.3>] [URL: <http://dx.doi.org/10.1063/1.3549932.4>]

result from the same instability mechanism. As before, the replacement of the leading eigenmode corresponds to the increase of the number of local minima in the central part of the cavity. Thus, in the stream function perturbation at  $L=10$ , the number of minima reaches 12. At the same time, there are some qualitative changes compared to the lower value of  $Hd$  (cf. Figs. 5 and 7). First, the maxima of the temperature perturbation appear to be much higher, which can be the main reason for increasing numerical resolution requirements. Second, contrary to the previous case, the maxima of stream function perturbation located near the vertical walls disappear with the increase of the aspect ratio, while the maxima stretched along the horizontal walls prevail. This can be connected with the development of Shercliff boundary layers along the horizontal boundaries that become more significant at stronger magnetic fields.

To finalize this section, we observe two qualitatively different patterns of perturbations, which show that there exist two main physical mechanisms that cause instability of steady flows. One is the characteristic for weaker magnetic field and longer cavity (e.g.,  $Hd=100$ ,  $L>5.6$ ) and the other one is the characteristic for shorter cavities or for stronger magnetic fields. As mentioned above, it is difficult to offer a clear physical explanation of these mechanisms. Some more insight, however, can be gained by observation of the real and imaginary parts of the most unstable perturbations and perturbation change during the period of oscillations (Fig. 8). In the first case [Fig. 8(a)], the oscillations are located near the vertical walls. A closer look (see also multimedia files) shows that perturbations appear as cold and hot spots in the lower left and upper right corners, advected by the flow and dissipating in the central part of the cavity. These spots cause oscillations of the stream function near the vertical walls. Far from these walls, velocity oscillations are weak. In the second case [Fig. 8(b)], we observe waves developing along the horizontal walls. The waves are advected along the horizontal boundaries from the centers toward the vertical walls,

where they disappear starting to ascend or descend with the flow. This is instability of the Shercliff boundary layers, which exhibits a similarity with instability of the boundary layers in convection of air, characteristic of a larger Prandtl number of 0.71, in tall vertical cavities [cf. Fig. 8(b) with plate 1 of Ref. 36]. Note also that the perturbation of the stream function in this case is much stronger than that of the temperature, so that we use more contrast coloring of the animation to make the temperature perturbation more visible. This indicates that the instability of boundary layers has mainly hydrodynamic origin.

## B. Stability for perfectly conducting horizontal boundaries

The dependence of the critical Grashof number and critical frequency on the aspect ratio for the case of perfectly conducting boundaries is shown in Fig. 9. Again, compared with the results for stability of flows unaffected by a magnetic field,<sup>34</sup> for which  $Gr_{cr} \approx 1.12 \times 10^5$ , we observe the stabilizing effect that increases with the increase of the field strength [cf. Figs. 9(a) and 9(c)]. Studying the stability diagrams (Fig. 9) and patterns of the most unstable perturbations (Figs. 10 and 11), we observe also that, compared with the case of insulating boundaries (Figs. 5–7), the flow stability properties differ qualitatively for the weaker magnetic field ( $Hd=100$ , Fig. 10) and are similar for the stronger one ( $Hd=1000$ , Fig. 11).

For a weaker magnetic field,  $Hd=100$ , there is only one instability mode that does not change qualitatively with the increase of the aspect ratio (Fig. 10). The corresponding neutral curve [Fig. 9(a)] and the dependence  $\omega_{cr}(L)$  [Fig. 9(b)] consist of a single continuous curve. Note that in the case of conducting horizontal boundaries, there are no thermal boundary layers near the vertical walls, so that the instability observed for smaller aspect ratios with the perfectly insulating walls (Fig. 6) cannot develop here. Patterns shown in

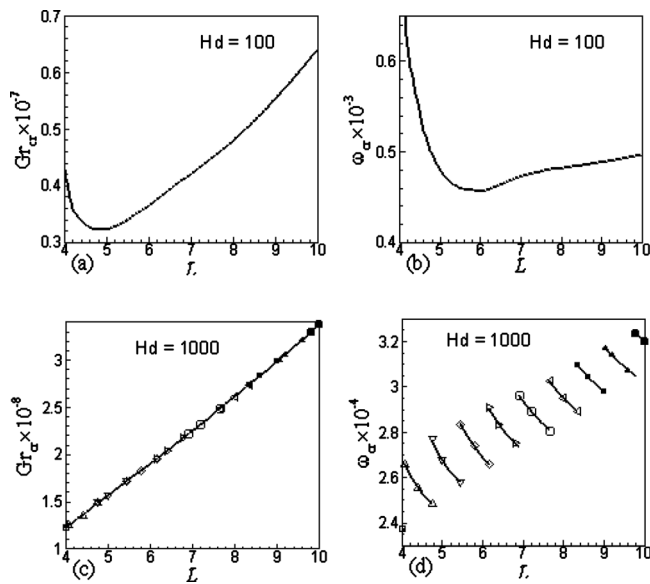


FIG. 9. Critical Grashof numbers and critical frequencies for oscillatory instability of steady flows in the case of perfectly thermally conducted horizontal boundaries. Different symbols in frames (c) and (d) correspond to different instability modes. Pr=0.015.

Fig. 10 illustrate a continuous change of perturbation with the increase of the aspect ratio. Since the temperature is prescribed at the horizontal boundaries, the temperature perturbation vanishes at all the boundaries. As a result, the cold and hot spots arise now closer to the horizontal centerline and, as in the case of insulating boundaries, are advected toward the cavity center where they dissipate. At stronger magnetic field, Hd=1000, we observe ten different perturbation modes that become dominant with the increase of the aspect ratio. Note that all modes continuously change with the governing parameters [see also Figs. 5(e) and 5(f)]. Each of the ten modes becomes leading for a certain interval of the aspect ratio values. These modes are similar to those observed for the perfectly insulated horizontal boundaries and correspond to the instability of Shercliff boundary layers. They are characterized by a strong perturbation of the stream function near the boundaries and a street of local minima located in the central part of the cavity. The number of minima changes with the change of the most unstable eigenmode and varies from 7 at L=4 to 16 at L=10 (Fig. 11). Similar to the case of insulated horizontal boundaries, these small perturbation structures travel along the horizontal boundaries. A closer look into time evolution of the perturbation (see multimedia files) reveals that, in this case, the stream function perturbations do not vanish near the boundaries, so that the instability of Shercliff boundary layers is observed along all four boundaries.

**C. Perturbation energy considerations**

Consider the linearized equations (28) and (29) at the critical values of parameters. Assuming that the leading eigenvalue is purely imaginary,  $\lambda = i\omega_{cr}$ , and that  $(\mathbf{v}, p, \theta)$  is the

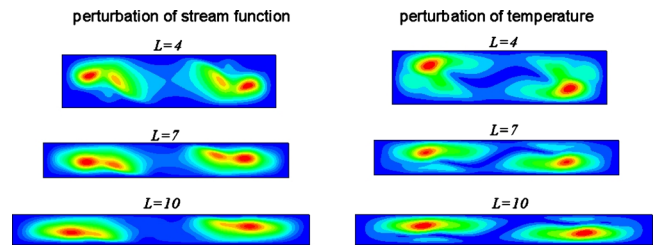


FIG. 10. (Color online) Absolute values of perturbation of stream function and temperature at Hd=100 belonging to the continuous critical curve at different aspect ratios. Perfectly conducting horizontal boundaries. Red (gray) color corresponds to the maximal values, blue (black) color corresponds to the zero values. Pr=0.015. (enhanced online).  
 [URL: <http://dx.doi.org/10.1063/1.3549932.5>]  
 [URL: <http://dx.doi.org/10.1063/1.3549932.6>]

corresponding leading eigenvector, we multiply Eqs. (28) and (30) by complex conjugates  $\mathbf{v}^*$  and  $\theta^*$ , respectively. This yields

$$i\omega|\mathbf{v}|^2 = -\nabla p \cdot \mathbf{v}^* + \nabla^2 \mathbf{v} \cdot \mathbf{v}^* - Hd|\mathbf{v}|^2 + Gr \theta \mathbf{e}_y \cdot \mathbf{v}^* - (\mathbf{V} \cdot \nabla) \mathbf{v} \cdot \mathbf{v}^* - (\mathbf{v} \cdot \nabla) \mathbf{V} \cdot \mathbf{v}^*, \tag{31}$$

$$i\omega|\theta|^2 = Pr^{-1} \nabla^2 \theta \cdot \theta^* - (\mathbf{V} \cdot \nabla) \theta \cdot \theta^* - (\mathbf{v} \cdot \nabla) \Theta \cdot \theta^*. \tag{32}$$

Following the commonly used notations, we interpret  $|\mathbf{v}|^2$  and  $|\theta|^2$  as measures of the perturbation energy (see, e.g., Ref. 2). The standard procedure of integration over the whole flow region  $\Omega$  results in

$$i\omega \int_{\Omega} |\mathbf{v}|^2 d\Omega = \int_{\Omega} \nabla^2 \mathbf{v} \cdot \mathbf{v}^* d\Omega - Hd \int_{\Omega} |\mathbf{v}|^2 d\Omega + Gr \int_{\Omega} \theta \mathbf{e}_y \cdot \mathbf{v}^* d\Omega - \int_{\Omega} (\mathbf{v} \cdot \nabla) \mathbf{V} \cdot \mathbf{v}^* d\Omega - \int_{\Omega} (\mathbf{V} \cdot \nabla) \mathbf{v} \cdot \mathbf{v}^* d\Omega, \tag{33}$$

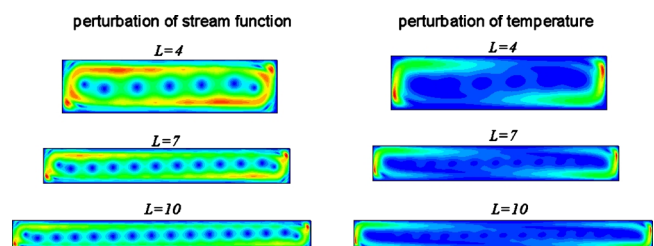


FIG. 11. (Color online) Absolute values of perturbation of stream function and temperature at Hd=1000 and aspect ratios corresponding to different branches of the neutral curve. Perfectly conducting horizontal boundaries. Red (gray) color corresponds to the maximal values, blue (black) color corresponds to the zero values. Pr=0.015. (enhanced online).  
 [URL: <http://dx.doi.org/10.1063/1.3549932.7>]  
 [URL: <http://dx.doi.org/10.1063/1.3549932.8>]

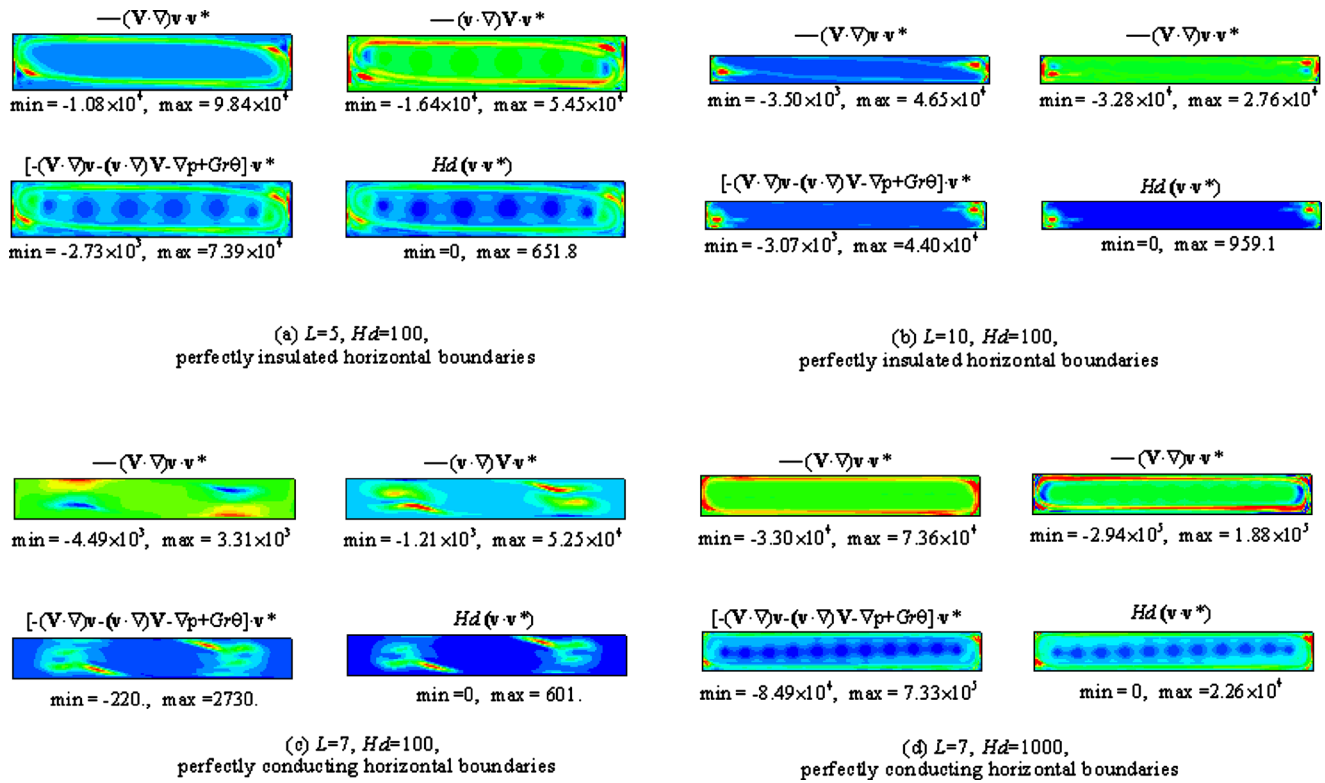


FIG. 12. (Color online) Imaginary parts of some terms of Eqs. (31) and (32) and real part of the term  $Hd(\mathbf{v} \cdot \mathbf{v})$  for several characteristic cases.

$$i\omega \int_{\Omega} |\theta|^2 d\Omega = Pr^{-1} \int_{\Omega} \nabla^2 \theta \cdot \theta^* d\Omega - \int_{\Omega} (\mathbf{v} \cdot \nabla) \theta \cdot \theta^* d\Omega - \int_{\Omega} (\mathbf{V} \cdot \nabla) \theta \cdot \theta^* d\Omega. \quad (34)$$

Note that since the eigenvector is a complex function, the last two terms of Eqs. (33) and (34) do not vanish, i.e.,  $(\mathbf{V} \cdot \nabla) \mathbf{v} \cdot \mathbf{v}^* \neq \mathbf{V} \cdot \nabla(|\mathbf{v}|^2/2)$  and  $(\mathbf{V} \cdot \nabla) \theta \cdot \theta^* \neq \mathbf{V} \cdot \nabla(|\theta|^2/2)$ . The equality holds only for real  $\mathbf{v}$  and  $\theta$ , for which the last terms of Eqs. (33) and (34) are zeros, as it happens in derivation of the classical Reynolds–Orr equation. Seemingly, this fact was overlooked in several previous stability studies, see, e.g., Refs. 13 and 14. Relations (33) and (34) describe the integral energy balance between the perturbation and the base state and can be easily verified numerically. Note that the exactness of the above equalities strongly depends on the mass and momentum conservation of a numerical scheme. The finite volume discretization used in this study is fully conservative, which allows us to transform integral equalities (33) and (34) into equalities with discrete summations. The latter is achieved if the same quadrature formulas are used for the discretization of governing equations and for the approximation of the integrals.

For the considered Q2D model and for the observed Hopf bifurcations, the relations (31)–(34) require a preliminary discussion. Apparently, the left-hand sides of all the equations are purely imaginary. Therefore, the real parts of the right-hand side (rhs) of all the equations are zeros. Moreover, according to Eqs. (31) and (32), they are zeros pointwise, i.e., the real parts of all the terms are pointwise bal-

anced and do not contribute to generation or dissipation of the perturbation energy even locally. Thus, in the figures below, we report mainly the imaginary parts of the terms. Moreover, the terms proportional to  $Hd$  in Eqs. (31) and (33) are purely real, and therefore are excluded from the energy balance either locally or globally. As it was shown above, these terms strongly affect the stability properties of the flow. It follows that energy considerations can give a comprehensive understanding of the observed instabilities. It allows us only to illustrate where the perturbation attains or dissi-

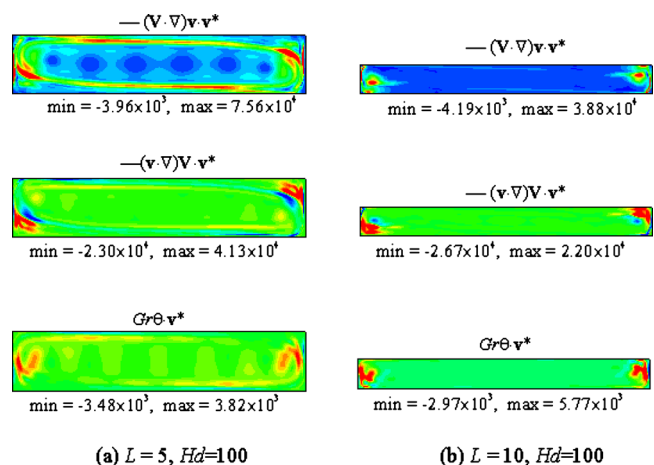


FIG. 13. (Color online) Imaginary parts of the divergent-free parts of non-divergent terms of Eqs. (31) and (32). Perfectly thermally insulated horizontal walls.

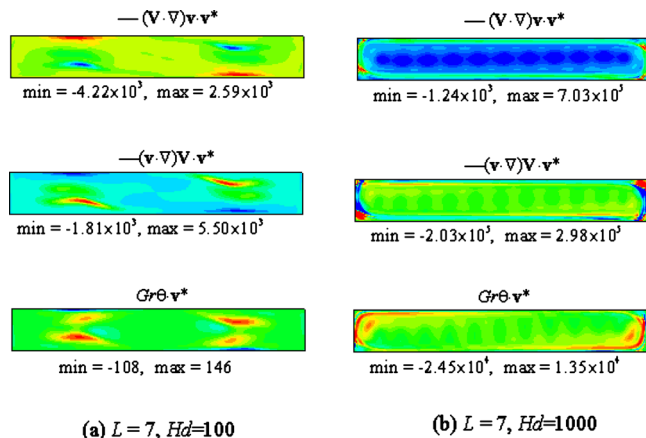


FIG. 14. (Color online) Imaginary parts of the divergent-free parts of non-divergent terms of Eqs. (31) and (32). Perfectly thermally conducting horizontal walls.

pates its energy, as well as to figure out which term of the momentum equation contributes more to the perturbation energy growth.

To illustrate the spatial patterns of the integrands of Eqs. (33) and (34) in the observed instabilities, we plot the imaginary parts of some terms of Eqs. (31) and (32) together with the real part of the term  $Hd(\mathbf{v} \cdot \mathbf{v})$  for four characteristic cases of the observed instabilities (Fig. 12). Note that the pattern of the latter term coincides with the pattern of the left-hand side (lhs) of Eq. (31) and therefore illustrates distribution of the perturbation kinetic energy. The amplitudes of the temperature perturbations were already plotted in Figs. 6, 7, 10, and 11. The parameter values in Fig. 12 were chosen to describe three different instability mechanisms illustrated in Fig. 6 and Figs. 10 and 11.

Patterns of Fig. 12 generally resemble what was already observed in the patterns of the perturbations themselves, i.e., growth of perturbations and their energy either in the boundary layers [Figs. 12(a), 12(b), and 12(d)] or in the bulk of the flow [Fig. 12(c)]. However, we argue that these patterns do not represent the production of perturbation energy correctly, and therefore are not those to be discussed. To show that, we plot the pattern of the sum of all the “production” terms of Eq. (31) from which the pressure gradient term is withdrawn. In other words, we plot the production of divergent-free part of the momentum equation. Comparing the corresponding frames of Fig. 12, we see that this production resembles the pattern of the lhs [coincides with  $Hd(\mathbf{v} \cdot \mathbf{v})$ ] of Eq. (31) in the almost whole flow region except boundary layers adjacent to the vertical walls, where the viscous dissipation is large. We

conclude that to discuss the contribution of each term of Eq. (31) to generation or dissipation of the perturbation energy, we need first to exclude the potential parts of each term. Clearly, the potential parts of the terms of momentum equation, full or linearized, are balanced by the pressure gradient and cannot play any role in the instability onset. On the other hand, if these parts are large, their amplitudes can overshadow the important effect of their divergence-free counterparts. It seems that this rather obvious observation also was overlooked in some previous studies (see, e.g., Refs. 13 and 14 and references therein).

To continue the energy analysis, we had calculated the divergence-free parts of all the nondivergent terms of the momentum equation shown in Fig. 12. After multiplication by  $\mathbf{v}^*$ , they yield physically meaningful parts of the integrands of Eq. (33) and are shown in Figs. 13 and 14. These patterns must be discussed in line with the perturbation patterns shown in Figs. 6–8, 10, and 11. We observe that in the cases when instability develops inside the boundary layers [Figs. 13(a), 13(b), and 14(b)], all the production terms steeply grow there as well. When the perturbation is located into the bulk of the flow [Fig. 14(a)], the production terms also grow steeply closer to the center indicating, however, that the kinetic energy production is shifted toward the horizontal boundaries where the base flow velocity is larger.

According to the above arguments, it will not be informative to compare the contribution of each term of the momentum equation into the energy production before the divergence-free parts are extracted. It is easy to see that the potential parts are cancelled already in Eq. (33) during the integrations, which are projections of the terms of the momentum equation on the divergent-free field  $\mathbf{v}^*$ . At the same time, plotting of each scalar component, say  $U \partial v / \partial x \cdot v^*$ , will leave the potential part into the vector components. Therefore, we first exclude the potential parts from the vectors  $(\mathbf{V} \cdot \nabla) \mathbf{v}$ ,  $(\mathbf{v} \cdot \nabla) \mathbf{V}$ , and  $Gr \theta \mathbf{e}_y$ , and only then study the contribution of the components of the results into the production of perturbation kinetic energy. The integral values for the cases of Fig. 12 are listed in Table II. Here we observe the domination of perturbation energy production by the term  $(\mathbf{V} \cdot \nabla) \mathbf{v}$  in the cases when instability develops in the boundary layers, which again indicates that this term is important for the energy balance. This production can be associated with the advection of perturbation along the boundaries, as it was observed in the perturbation patterns and snapshots. For instability developing in the bulk of the flow, we observe the domination of the term  $(\mathbf{v} \cdot \nabla) \mathbf{V}$ , which describes the advection of the mean flow by the perturbation velocity. The sharp maxima in the corresponding frame of

TABLE II. Imaginary parts of the divergence-free components of the rhs terms of Eq. (33).

Case	$-\left[(\mathbf{V} \cdot \nabla) \mathbf{v}\right]_x \cdot u^*$	$-\left[(\mathbf{v} \cdot \nabla) \mathbf{V}\right]_x \cdot u^*$	$-\left[(\mathbf{V} \cdot \nabla) \mathbf{v}\right]_y \cdot v^*$	$-\left[(\mathbf{v} \cdot \nabla) \mathbf{V}\right]_y \cdot v^*$	$Gr \theta \cdot v^*$
$L=5$ , $Hd=100$ , $Gr=3.07 \times 10^7$ , insulated horizontal walls	$2.920 \times 10^4$	1152	$1.185 \times 10^4$	1634	1299
$L=10$ , $Hd=100$ , $Gr=3.69 \times 10^7$ , insulated horizontal walls	$1.129 \times 10^4$	2116	5500	1505	1198
$L=7$ , $Hd=100$ , $Gr=4.21 \times 10^6$ , conducting horizontal walls	-691.2	2193	-165.9	652.1	62.03
$L=7$ , $Hd=1000$ , $Gr=2.25 \times 10^8$ , conducting horizontal walls	$1.159 \times 10^5$	-2852	$4.422 \times 10^4$	3192	2999

Fig. 14(a) illustrate the domination of this term. The location of these maxima corresponds to the area of strong flow oscillations, as illustrated by the snapshots in Fig. 8.

## VI. CONCLUSIONS

The Q2D model of convective flows under the effect of a transverse magnetic field has been studied numerically. The numerical method has been verified by a comprehensive convergence study and a comparison with the analytical results obtained for the Rayleigh–Bénard configuration. To validate the model, a qualitative agreement with recently published experiments has been obtained.

Patterns of steady state flows and their stability have been studied for fixed values of the scaled Hartmann number,  $Hd=100$  and  $1000$ . The parametric dependence of critical Grashof number and critical frequency on the box aspect ratio varying between  $L=4$  and  $L=10$  was obtained, while the box horizontal boundaries were considered to be either perfectly thermally insulating or perfectly conducting.

We observed that multiple many-cell steady flow states characteristic of flows in long horizontal cavities<sup>34</sup> are suppressed by the magnetic field, so that only single-cell steady flows are observed. Along with the instability of the bulk flow observed in the absence of the magnetic field, these single-cell flows can be destabilized by two additional instability mechanisms. The first one is characterized by the appearance of cold and hot spots near the vertical boundaries that are advected into the central part of the flow where they dissipate. This mechanism is observed at  $Hd=100$  for all aspect ratios in the case of perfectly conducting horizontal boundaries and for  $Hd=100$  and  $L < 5.6$  for perfectly insulated horizontal boundaries.

The second mechanism, characteristic of stronger magnetic fields ( $Hd=1000$ ), as well as for  $L > 5.6$ ,  $Hd=100$ , and perfectly insulated horizontal boundaries, exhibits some features similar to what was already observed in flows affected by vertical or transverse magnetic field, as well as convective flows of fluids with a larger Prandtl number. The strong transverse magnetic field stabilizes the flow by suppressing perturbations in the central part of the cavity. The instability sets in thin thermal and Shercliff boundary layers located near the heated, cooled, and horizontal boundaries. The perturbation pattern and the resulting oscillation frequency depend on the ratio of boundary layer thickness and the cavity length. The boundary layers tend to become thinner with the increase of the Hartmann number and to elongate with the increase of the aspect ratio. The thinning and elongation, in their turn, change the perturbation pattern, which can remain qualitatively the same but contains a different number of small structures. The latter is most strongly emphasized at large Hartmann numbers,  $Hd=1000$  and beyond, and for the thermally insulating horizontal boundaries.

We have argued that consideration of the production and dissipation of perturbation energy yields only a partial description of the observed instabilities and cannot help in their comprehensive understanding. We also discussed several important issues of this analysis that seemingly were overlooked in some previous studies. In particular, we argued that

before energy production by a term of the governing equations is computed, its potential part must be excluded from the consideration. In the current study, after the divergent-free parts were excluded from all the terms, their patterns resembled the observations already made for the patterns of leading disturbances. The computation of the integral contribution of the terms over the whole flow region showed that in the cases when instability develops in the boundary layers, the energy production by the term  $(\mathbf{V} \cdot \nabla)\mathbf{v}$  dominates. When the instability develops in the bulk of the flow, the term  $(\mathbf{v} \cdot \nabla)\mathbf{V}$  produces the largest amount of the perturbation energy.

## ACKNOWLEDGMENTS

This research was supported by the Ministry of Science and Technology, Israel, Grant No. 3-5689. Large-scale calculations have been performed at a high performance cluster based at the Faculty of Engineering and Computing of Coventry University. The authors are indebted to Applied Mathematics Research Centre of Coventry University for providing this opportunity.

- <sup>1</sup>M. R. E. Proctor and N. O. Weiss, “Magnetoconvection,” *Rep. Prog. Phys.* **45**, 1317 (1982).
- <sup>2</sup>M. Lappa, *Thermal Convection* (Wiley, New York, 2009), p. 670.
- <sup>3</sup>*Crystal Growth under Applied Fields*, edited by S. Dost and Y. Okano (Transworld Research Network, Kerala, India, 2007), p. 214.
- <sup>4</sup>A. Yu. Gelfgat, P. Z. Bar-Yoseph, and A. Solan, “Effect of axial magnetic field on three-dimensional instability of natural convection in a vertical Bridgman growth configuration,” *J. Cryst. Growth* **230**, 63 (2001).
- <sup>5</sup>A. Yu. Gelfgat and P. Z. Bar-Yoseph, “The effect of an external magnetic field on oscillatory instability of convective flows in a rectangular cavity,” *Phys. Fluids* **13**, 2269 (2001).
- <sup>6</sup>D. T. J. Hurle and R. W. Series, “Use of magnetic field in melt growth,” *Handbook of Crystal Growth* (Elsevier, New York, 1994), Vol. 2, p. 260.
- <sup>7</sup>S. Aleksandrova, “Buoyant convection in cavities in a strong magnetic field,” Ph.D. thesis, Coventry University, 2001.
- <sup>8</sup>S. Aleksandrova and S. Molokov, “Three-dimensional buoyant convection in a rectangular cavity with differentially heated walls in a strong magnetic field,” *Fluid Dyn. Res.* **35**, 37 (2004).
- <sup>9</sup>*Magnetohydrodynamics: Historical Evolution and Trends*, edited by S. Molokov, R. Moreau, and H. K. Moffatt (Springer, New York, 2007).
- <sup>10</sup>H. Ozoe, *Magnetic Convection* (Imperial College Press, London, 2005).
- <sup>11</sup>U. Burr and U. Müller, “Rayleigh–Bénard convection in liquid metal layers under the influence of a horizontal magnetic field,” *J. Fluid Mech.* **453**, 345 (2002).
- <sup>12</sup>G. Authié, T. Tagawa, and R. Moreau, “Buoyant flow in long vertical enclosures in the presence of a strong horizontal magnetic field. Part 2. Finite enclosures,” *Eur. J. Mech. B/Fluids* **22**, 203 (2003).
- <sup>13</sup>D. Henry, A. Juel, H. Ben Hadid, and S. Kaddesche, “Directional effect of a magnetic field on oscillatory low-Prandtl-number convection,” *Phys. Fluids* **20**, 034104 (2008).
- <sup>14</sup>D. V. Lyubimov, T. P. Lyubimova, A. B. Perminov, D. Henry, and H. Ben Hadid, “Stability of convection in a horizontal channel subjected to a longitudinal temperature gradient,” *J. Fluid Mech.* **635**, 297 (2009).
- <sup>15</sup>U. Burr, L. Barleon, P. Jochmann, and A. Tsinober, “Magnetohydrodynamic convection in a vertical slot with horizontal magnetic field,” *J. Fluid Mech.* **475**, 21 (2003).
- <sup>16</sup>B. Hof, A. Juel, and T. Mullin, “Magnetohydrodynamic damping of oscillations in low-Prandtl-number convection,” *J. Fluid Mech.* **545**, 193 (2005).
- <sup>17</sup>H. Ben Hadid and D. Henry, “Numerical study of convection in the horizontal Bridgman configuration under the action of a constant magnetic field. Part 2. Three-dimensional flow,” *J. Fluid Mech.* **333**, 57 (1997).
- <sup>18</sup>J. C. R. Hunt, “Magnetohydrodynamic flow in rectangular ducts,” *J. Fluid Mech.* **21**, 577 (1965).
- <sup>19</sup>J. Priede, S. Aleksandrova, and S. Molokov, “Linear stability of Hunt’s flow,” *J. Fluid Mech.* **649**, 115 (2010).

- <sup>20</sup>M. Kinet, B. Knaepen, and S. Molokov, "Instabilities and transition in magnetohydrodynamic flows in ducts with electrically conducting walls," *Phys. Rev. Lett.* **103**, 154501 (2009).
- <sup>21</sup>J. S. Walker, "Magnetohydrodynamic flows in rectangular ducts with thin conducting walls," *J. Mec.* **20**, 79 (1981).
- <sup>22</sup>S. Molokov and L. Bühler, "Liquid-metal flow in a U-bend in a strong uniform magnetic field," *J. Fluid Mech.* **267**, 325 (1994).
- <sup>23</sup>R. Stieglitz, L. Barleon, L. Bühler, and S. Molokov, "Magnetohydrodynamic flow in a right angle bend in a strong magnetic field," *J. Fluid Mech.* **326**, 91 (1996).
- <sup>24</sup>T. Q. Hua and J. S. Walker, "Three-dimensional MHD flow in circular ducts in non-uniform, transverse magnetic fields," *Int. J. Eng. Sci.* **27**, 1079 (1989).
- <sup>25</sup>S. Molokov and C. B. Reed, "Parametric study of the liquid metal flow in a straight insulated circular duct in a strong nonuniform magnetic field," *Fusion Sci. Technol.* **32**, 200 (2003).
- <sup>26</sup>R. Moreau and S. Molokov, "Julius Hartmann and his followers: A review on the properties of the Hartmann layer," in *Magnetohydrodynamics: Historical Evolution and Trends*, edited by S. Molokov, R. Moreau, and H. K. Moffatt (Springer, New York, 2007), p. 155.
- <sup>27</sup>J. Sommeria and R. Moreau, "Why, how, and when, MHD turbulence becomes two-dimensional," *J. Fluid Mech.* **118**, 507 (1982).
- <sup>28</sup>L. Bühler, "Instabilities in quasi-two-dimensional magnetohydrodynamic flows," *J. Fluid Mech.* **326**, 125 (1996).
- <sup>29</sup>I. V. Lavrentiev, S. Molokov, S. I. Sidorenkov, and A. Shishko, "Stokes flow in a rectangular magnetohydrodynamic channel with nonconducting walls within a nonuniform magnetic field at large Hartmann numbers," *Magnetohydrodynamics (N.Y.)* **26**, 328 (1990).
- <sup>30</sup>T. Alboussière, "A geostrophic-like model for large-Hartmann-number flows," *J. Fluid Mech.* **521**, 125 (2004).
- <sup>31</sup>A. Pothérat, J. Sommeria, and R. Moreau, "An effective two-dimensional model for MHD flows with transverse magnetic field," *J. Fluid Mech.* **424**, 75 (2000).
- <sup>32</sup>A. Pothérat, J. Sommeria, and R. Moreau, "Numerical simulations of an effective two-dimensional model for flows with a transverse magnetic field," *J. Fluid Mech.* **534**, 115 (2005).
- <sup>33</sup>M. Frank, L. Barleon, and U. Müller, "Visual analysis of two-dimensional magnetohydrodynamics," *Phys. Fluids* **13**, 2287 (2001).
- <sup>34</sup>A. Yu. Gelfgat, P. Z. Bar-Yoseph, and A. L. Yarin, "Stability of multiple steady states of convection in laterally heated cavities," *J. Fluid Mech.* **388**, 315 (1999).
- <sup>35</sup>"Numerical simulation of oscillatory convection in low-Pr fluids: A GAMM workshop," *Notes on Numerical Fluid Mechanics*, edited by B. Roux (Vieweg, Braunschweig, 1990), Vol. 27.
- <sup>36</sup>S. Xin and P. Le Quéré, "An extended Chebyshev pseudo-spectral benchmark for the 8:1 differentially heated cavity," *Int. J. Numer. Methods Fluids* **40**, 981 (2002).
- <sup>37</sup>A. Yu. Gelfgat, "Stability of convective flows in cavities: Solution of benchmark problems by a low-order finite volume method," *Int. J. Numer. Methods Fluids* **53**, 485 (2007).